Nano Research

Open Access

Research Article

Ultrahigh loading of confined plasmonic nanoparticles within thiol-functionalized metal-organic frameworks for efficient photocatalytic CO_2 reduction to CO and hydrocarbons

Jinzhou Chen[1,2,§], Yanhui Su[1,2,§], Yuhan Wang[1,2], Zhihe Wei[1,2], Zhangyi Zheng[1,2], Huihong Yuan[1,2], Zhenyang Jiao[1,2], Zhao Deng[1,2], Wenjun Yang[1,2] ✉, and Yang Peng[1,2] ✉

[1] *Soochow Institute for Energy and Materials Innovations, College of Energy, Key Laboratory of Advanced Carbon Materials and Wearable Energy Technologies of Jiangsu Province, Soochow University, Suzhou 215006, China*
[2] *Jiangsu Key Laboratory of Advanced Negative Carbon Technologies, Soochow University, Suzhou 215123, China*
[§] *Jinzhou Chen and Yanhui Su contributed equally to this work.*

Cite this article: *Nano Research*, **2025**, *18*, 94907181. https://doi.org/10.26599/NR.2025.94907181

ABSTRACT: Porous materials can serve as optimal supporters for the fabrication of confined plasmon nano-photocatalysts with high dispersity. The low-loading amounts of the confined nanoparticles (NPs) due to their easy-to-migrate tendency out of the pores, however, cause a bottleneck for the photocatalytic performance. We herein reported the *in-situ* growth of Ag NPs within thio-functionalized UiO-66 metal-organic frameworks (MOFs). Owing to the anchoring effects of the thiol groups, Ag nanoparticles were stabilized in the channels at ultrahigh loading amounts (up to 51.2%) for significantly enhanced plasmonic resonance. Through optimizing the loading amounts of confined Ag and the remaining pore volumes for mass diffusion, we achieved an exceptional catalytic activity for the photocatalytic reduction of CO_2 with Ag@MOFs. The photo-induced electron transfer rate is as high as 142.4 μmol·g^{-1}·h^{-1}, which is ~ 17.4 times higher than bare UiO-66-$(SH)_2$. Notably, the enhanced charge transfer kinetics, facilitated by the plasmon-induced hot-electron injections, enables the multiple-electron reduction of CO_2 to hydrocarbons. This work presents a straightforward strategy for constructing confined plasmon NPs with ultrahigh loading amounts, and demonstrates their remarkable performance in photocatalytic CO_2 reduction.

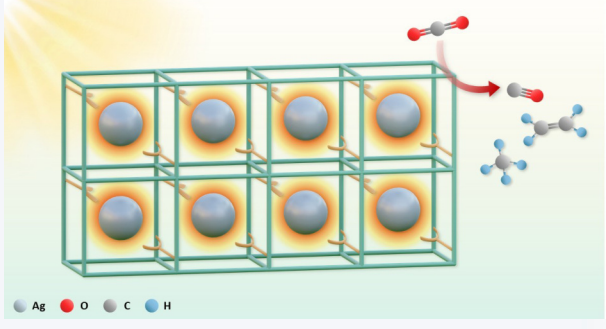

KEYWORDS: photocatalytic CO_2 reduction, metal-organic frameworks, plasmonic resonance, nanoparticle migration, hot electron

1 Introduction

Sunlight-driven conversion of CO_2 to hydrocarbon fuel offers an appealing route to store intermittent solar energy into chemical energy while approaching carbon neutrality [1–7]. Semiconductors with suitable band structures have been demonstrated as the workhorse of the photocatalysts in CO_2 reduction [8, 9]. Nevertheless, the poor visible/infrared-light response and the low-efficient energy coupling into CO_2 conversion hamper their shift to practical applications [10–13]. The selective transformation to hydrocarbons that requires high kinetics of multiple-electron transfer represents another challenge [14].

Plasmonic metal nanoparticles (NPs) recently exhibit great potentials for efficient photoconversion. Its interaction with incident photons can induce collective oscillation of electrons, i.e., localized surface plasmon resonance (LSPR) [15, 16]. The light energy will be collected and accumulated on nanoparticle surface in the form of enhanced electromagnetic filed. The localized filed can promote the resonance energy transfer or hot electron injection [17]. Besides, the absorption wavelength of LSPR can extend from visible to near-infrared range depend on the morphology of plasmonic NPs. Owing to the energetic charge carriers and broad solar-light harvesting, plasmonic materials have been widely used in photocatalytic CO_2 reduction and can significantly enhance the reaction kinetics and energy utilization efficiency [18–20].

Received: October 6, 2024; **Revised:** December 5, 2024
Accepted: December 11, 2024

✉Address correspondence to Wenjun Yang, wjyang@suda.edu.cn; Yang Peng, ypeng@suda.edu.cn

However, the low affinities of plasmonic metal NPs to CO_2 can retard the gas-reduction reactions.

Porous metal-organic frameworks (MOFs) feature excellent CO_2 adsorption abilities and can serve as a three-dimensional support matric for hosting surface-clean metal NPs [21]. The encapsulation of plasmon NPs into MOFs would not only concentrate CO_2 around the catalytic centers, but also stabilize the metal NPs with high dispersity. Nevertheless, the high migration tendency of NPs to the surface of MOFs supporter under synthesis conditions, restricts the loading of the confined plasmonic NPs < 20%, and consequently hampers the overall catalytic performance [22]. Herein, we report ultrahigh-loaded Ag@MOFs composites for highly efficient photocatalytic CO_2 reduction. The MOFs supporters are functionalized with thiol groups to enhance its interactions with the encapsulated Ag NPs, restricting their leaching from pores. The resulting composites achieve ultrahigh loading amounts of Ag NPs and exhibit significantly enhanced photocatalytic activities. Specifically, Ag@MOFs furnishes an excellent yield of 128.0 μmol·g^{-1} for CO_2-to-CO photocatalytic reduction, 7.7 times higher than that of bare UiO-66. Moreover, highly electron-demanding hydrocarbon products are produced as well due to the generation of highly-energetic hot electrons.

2 Results and discussion

The schematic illustration for the preparation procedure of Ag@UiOS is shown in Fig. 1(a). UiO-66-$(SH)_2$ was prepared by the solvothermal reaction of $ZrCl_4$ with a bifunctional building block-*p*-mercaptoterephthalic acid, of which the carboxyl groups coordinate with Zr(IV) center to form the MOF skeleton, and thiol groups can effectively capture metal ions. Ag^+ was subsequently encapsulated into UiO-66-$(SH)_2$ using solution impregnation method followed by the *in-situ* reduction with ethanol under Xenon lamp illumination for 16 h. The morphology of resulting Ag@UiOS was

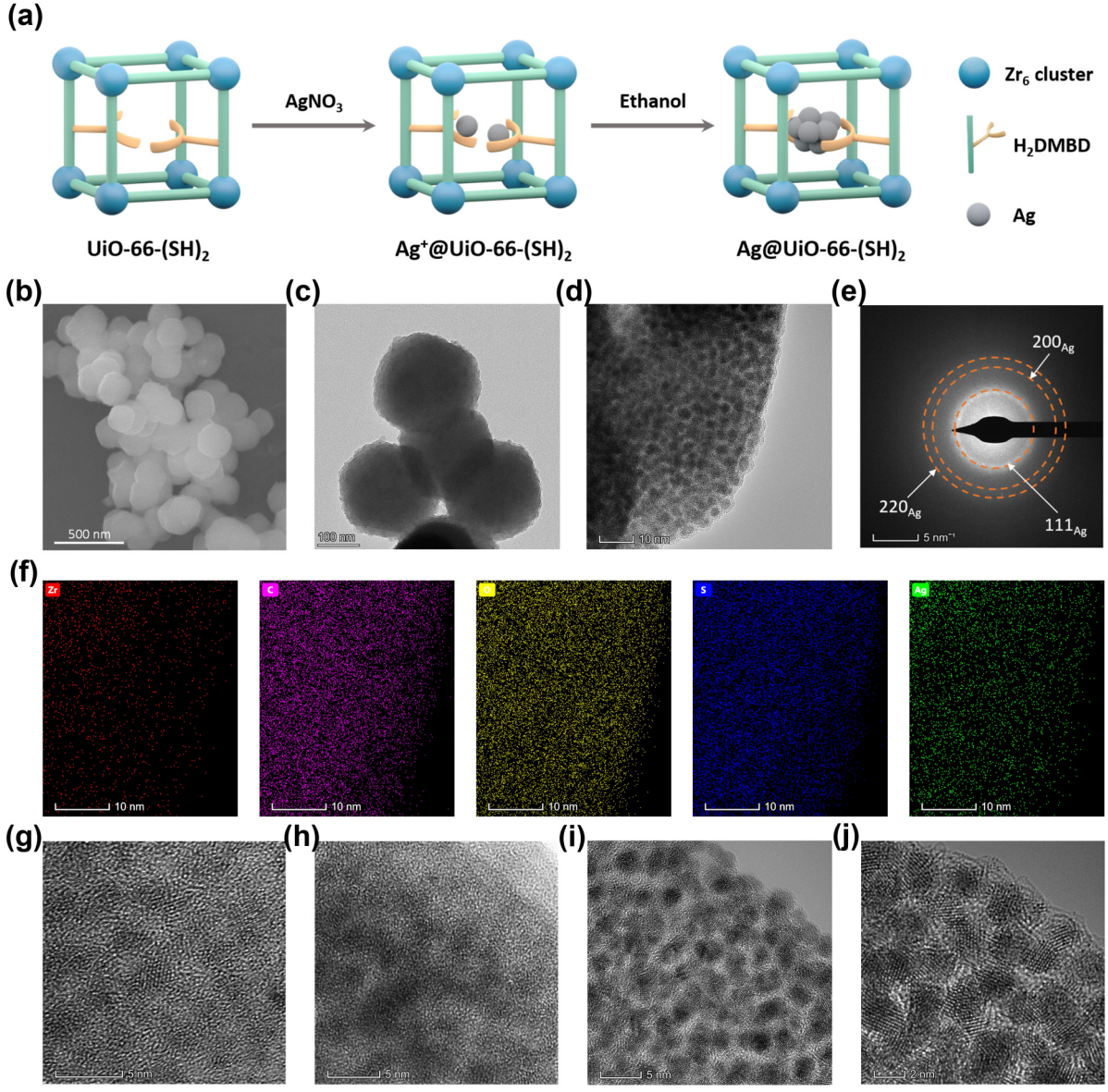

Figure 1 Characterization of Ag@UiOS synthesized using the "ship in a bottle" approach. (a) Schematic diagram of the synthesis process of Ag@UiOS material. (b) SEM, (c) TEM, (d) cross-sectional AC-TEM, (e) SAED, and (f) cross-sectional AC-TEM mapping images of Ag_1@UiOS. (g)–(j) Cross-sectional AC-TEM images corresponding to $Ag_{0.2}$@UiOS, $Ag_{0.5}$@UiOS, Ag_1@UiOS, and Ag_2@UiOS.

characterized by scanning electron microscopy (SEM), transmission electron microscopy (TEM), and spherical aberration-corrected transmission electron microscopy (AC-TEM). SEM and TEM show that the morophogy of Ag@UiOS (Figs. 1(b) and 1(c)) stay the same as the parent UiO-66-$(SH)_2$ (Fig. S1(a) in the Electronic Supplementary Material (ESM)). Both of the particles have smooth surface and octahedral shapes with a size distribution of around 250 nm, indicating the successful confinement of Ag particles and no leaching to the surface of MOF. Cross-sectional AC-TEM images of Ag@UiOS show that the Ag particles in MOF matrix are of a narrow size distribution of several nanometers (Fig. 1(d)). Selected-area electron diffraction (SAED) confirms that Ag(111), (200), and (220) crystal facets are mainly exposed (Fig. 1(e)). Uniform distributions of Zr, C, O, S, and Ag are observed in cross-sectional AC-TEM mapping (Fig. 1(f)), further proving the successful encapulsation of Ag particles in MOF. The loadings of Ag NPs can be elevated by adding more $AgNO_3$ precursor. We prepared a series of ultrahigh-loaded samples with 8.32%, 23.27%, 39.79%, and 51.20% Ag, denoted as $Ag_{0.2}$@UiOS, $Ag_{0.5}$@UiOS, Ag_1@UiOS, and Ag_2@UiOS (Table S1 in the ESM). Notably, the Ag particle sizes increase slightly with the loading amounts as revealed by the cross-sectional AC-TEM images (Figs. 1(g)–1(j)). The average sizes of the Ag particles in $Ag_{0.2}$@UiOS, $Ag_{0.5}$@UiOS, Ag_1@UiOS, and Ag_2@UiOS are determined as 1.06, 1.9, 2.0, and 5.0 nm, respectively (Figs. S2–S5 in the ESM). Moreover, no migration of Ag NPs to the surface of MOFs was observed even for Ag_2@UiOS. As a reference, we conducted the same encapsulation process within non-founctionalized UiO-66 with the Ag:UiO-66 ratios as 1:5, 1:1, and 2:1. The SEM images of the samples all show the leaching of Ag NPs to the surface (Fig. S6 in the ESM). We therefore suppose that the upper limitation of the Ag loadings for non-functionalized UiO-66 is < 20%, which highlight the advantages of the –SH groups of UiO-66-$(SH)_2$ on stabilizing the ultra-high loaded Ag NPs in the pore channels. The encapsulations of other plasmonic metals, i.e., Au and Cu, were performed. The TEM and mapping images of prepared Au@UiOS and Cu@UiOS both confirm the homogeneous encapsulation of the metals in MOFs, and exclude their leaching onto the surface (Figs. S7 and S8 in the ESM). Our fabrication strategy of metal@MOFs thus has broad applicability.

The X-ray diffraction (XRD) results indicate that UiO-66-$(SH)_2$ possesses *fcu* topology with each of the octahedral $Zr_6O_4(OH)_4$ SBU connected to 12 of its neighbors through the terephthalate linkers (Fig. 2(a)). The peaks at 7.3° and 8.4° correspond to the (111) and (200) facets of the crystals, respectively. The gradual drop and the final disappearance of the (111) facet signal, that represents the characteristic pore structure of UiO-66-$(SH)_2$, with the increase of Ag loading, confirm that Ag particles are positioned in the pores of MOF, as also revealed by the significant decrease of surface area from 432 to 18 $m^2 \cdot g^{-1}$ in Brunauer–Emmett–Teller (BET) analysis (Fig. S7 in the ESM). The XRD patterns of all the Ag@UiOS samples exhibit no peaks related to crystal (fcc) Ag, which strengthens the conclusion that Ag particles are too small to produce Bragg diffraction peaks. In the infrared spectra, we observed the complete disappearance of the vibration peak of –SH at 2570 cm^{-1} after the introduction of Ag [23] (Fig. 2(b)). In addition, the C=C vibration peak of benzene ring at 1273 cm^{-1} undergoes a red shift of about 20 cm^{-1} from sample UiO-66-$(SH)_2$ to Ag_2@UiOS, while the vibration bands of carboxyl group at 1403 and 1585 cm^{-1}, far away from the –SH group in the *p*-mercaptoterephthalic acid, display less pronounced red shifts. These results reveal the presence of Ag–S bonds, attaining the crucial role of –SH group on anchoring the Ag particles. The CO_2 adsorption results reveal the high CO_2 capacity of UiO-66-$(SH)_2$, which can promote the mass transfer of the reaction (Fig. S8 in the ESM). However, this capacity undergoes a linear drop with the loading of Ag NPs due to the reduced pore volumes and surface areas (Fig. S10 in the ESM).

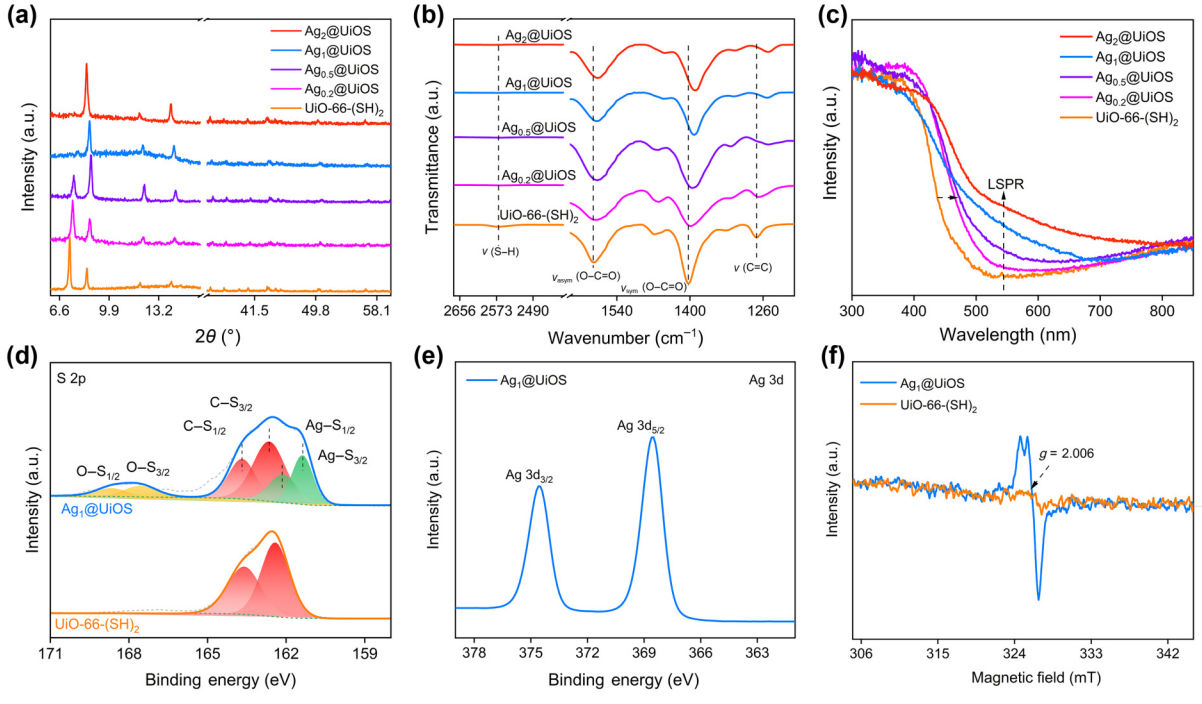

Figure 2 Series characterization of UiO-66-$(SH)_2$ and Ag_x@UiOS. (a) XRD pattern, (b) Fourier transform infrared (FT-IR) spectra, (c) UV–vis diffuse reflection spectra, (d) high-resolution XPS spectra of S 2p, (e) high-resolution XPS spectrum of Ag 3d, and (f) ESR spectra.

We further investigated the optical properties and electronic structures of Ag@UiOS by ultraviolet–visible (UV–vis) diffuse reflectance spectroscopy, X-ray photoelectron spectroscopy (XPS), and electron spin resonance (ESR). The UV–vis spectra show that the encapsulation of Ag effectively extends the absorption range to the visible region with the characteristic LSPR peak of Ag located at around 550 nm (Fig. 2(c)). The stepwise rise of the LSPR peak from $Ag_{0.2}$@UiOS to Ag_2@UiOS also indicates the enhancement of their plasmonic effect. The XPS spectra of Ag@UiOS samples given in Fig. S9 in the ESM confirm the presence of C, N, O, S, Zr, and Ag elements. The high-resolution S 2p spectrum of bare UiO-66-$(SH)_2$ shows the binding signals of free thiols at 162.4 and 163.6 eV (Fig. 2(d), bottom). In comparison, the S 2p spectrum of Ag@ UiO-66-$(SH)_2$ sample exhibits two extra groups of peaks at ~ 160–163 and ~ 166–170 eV that represent Ag–S and oxidized sulfur components, respectively [24], supporting the chemical interactions between Ag NPs and thiol-tethered MOF. The sharp Ag $3d_{3/2}$ (374.5 eV) and Ag $3d_{5/2}$ (368.5 eV) binding signals in the Ag 3d spectrum indicate that the oxidation states of encapsulated Ag are mainly zero [25] (Fig. 2(e)). The peak at about g = 2.006 in ESR is the isotropic paramagnetic peak of Ag^0, which also proves its valence state [26] (Fig. 2(f)).

The photocatalytic CO_2 reduction performance of the prepared samples was evaluated in a solid–gas system under 300 W xenon lamp illumination (859 mW·cm^{-2}) at a pressure of 0.3 MPa with H_2O as the electron donor. As shown in Fig. 3(a), the full-spectrum illumination of UiO-66-$(SH)_2$ furnished a low CO yield of 4.1 μmol·g^{-1}·h^{-1} due to the narrow adsorption wavelength. In contrast, the reaction with Ag_1@UiOS exhibited a ~ 7.8-folds elevation (32.0 μmol·g^{-1}·h^{-1}) in CO production. Strikingly, highly electron-demanding products C_xH_y were additionally obtained in 9.8 μmol·g^{-1}·h^{-1} with Ag_1@UiOS, indicating a significant enhancement of charge transfer efficiency endowed by the plasmonic Ag NPs. Such enhancement depends on the loading amounts of Ag NPs. From $Ag_{0.2}$@UiOS to Ag_1@UiOS, the yields of CO and C_xH_y, as well as the total photoelectron numbers for CO_2 reductions under full-spectrum irradiation were significantly elevated (Figs. 3(a) and 3(b)). Further increase of the Ag NPs loading amounts to 51.2 % (Ag_2@UiOS) however found the drop of photocatalytic yields, which could be ascribed to the limitation of mass diffusion (Figs. S9–S11 in the ESM). Apparently, the loading of plasmon NPs and residual pore volumes within the MOFs should be balanced for an optimal catalytic kinetics. The more profound enhancement of C_xH_y selectivity at λ > 490 nm, beyond the absorption range of the MOF, further validates the role of plasmonic Ag in driving the deep reductions of CO_2 (Fig. 3(c)). Finally, the optimal Ag_1@UiOS furnished an CO production rate of 32 with 142 μmol·g^{-1}·h^{-1} electron transfer yield, which represents a remarkable performance among the relevant literature (Fig. 3(d) and Table S2 in the ESM). The controlled experiments were conducted without catalyst or under dark (Fig. S13 in the ESM), which all furnished no gas product, confirming the indispensable role of the photocatalyst and the light source. To probe the carbon source of CO and hydrocarbon product, an isotope labelling experiment was carried out under the atmosphere of $^{13}CO_2$, and the gas products were analyzed by series gas chromatography-mass spectrometry (GC-MS). Only labelling peaks of ^{13}CO at m/z = 29, $^{13}CH_4$ at m/z = 17, and $^{13}C_2H_4$ at m/z = 30 were observed, strongly suggesting that the photocatalytic products derived from CO_2 (Fig. S14 in the ESM). The stability test of Ag@UiOS showed partial degradation of catalytic activity after five cycles (Fig. S15 in the ESM). The XRD characterization of the post-photoreaction catalysts exhibited the collapse of the structure (Fig. S16 in the ESM), rationalizing the performance degradation in cycle tests. To study the practical applicability of the photocatalytic system, we performed the CO_2 reduction experiment under natural sunlight. However, Ag_1@UiOS gave a CO production rate of 18 μmol·g^{-1}·h^{-1} along with trace C_xH_y, which was lower compared to the

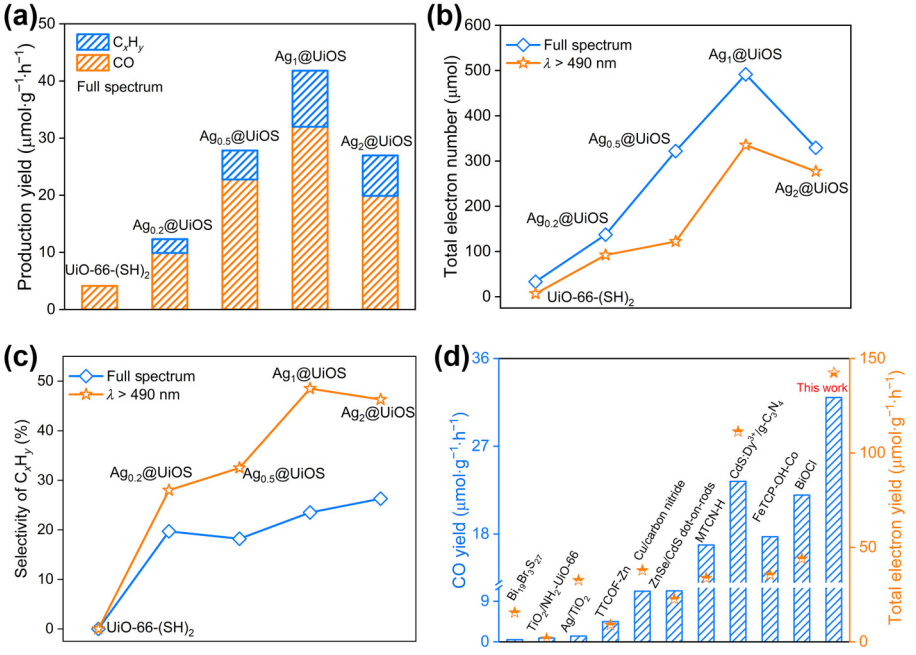

Figure 3 Photocatalytic performance of Ag@UiOS. (a) Comparison of the photocatalytic CO_2 reduction performance of Ag@UiOS under full spectrum condition. (b) Comparison of the total electron transfer numbers in the photocatalytic CO_2 reduction of Ag@UiOS under full spectrum (over a 4 h period) condition. (c) Comparison of the photocatalytic CO_2 reduction selectivity of Ag@UiOS under full spectrum (over a 4 h period) and λ > 490 nm (over a 24 h period) conditions. (d) Performance comparison with literature in the field. Note: the references for the data are shown in Table S2 in the ESM.

performance obtained under Xenon lamp illumination (Fig. S17 in the ESM). We attribute this to the much lower light intensity in average caused by cloud blockage.

The successful achievement of the multi-electron CO_2 reductions prompted a further investigation on the role of Ag NPs. We first probed the band structure of the catalyst through UV–vis diffuse reflectance spectroscopy (Fig. S15 in the ESM) and ultraviolet photoelectron spectroscopy (Fig. S16 in the ESM). As depicted in the band structure diagram (Fig. S17 in the ESM), bare UiO-66-$(SH)_2$ presents n-type characteristics with the Fermi level calculated as –0.56 V (vs. normal hydrogen electrode (NHE)), largely higher than that of Ag NPs. The contact with Ag will therefore cause the interfacial charge transfer from UiO-66-$(SH)_2$ to Ag and eventually an upward band bending, known as Schottky barrier [27]. This is supported by the drop of the Fermi level and elevation of the valance band from UiO-66-$(SH)_2$ to Ag_1@UiOS. The formation of Schottky barrier should enhance the transfer efficiency of photogenerated electrons within the composite (Fig. 4(a)) [28]. Indeed, the encapsulation of Ag NPs causes the significant decrease of photoluminescence emission peak of UiO-66-$(SH)_2$ center at 492 nm, which implies the effective suppression on the recombination of photoinduced electron-hole pairs. Moreover, the quenching effects of the luminescence were found to elevate with the loading amounts of the Ag NPs, revealing the enlargement of contacting area between Ag and MOF. Notably, a shoulder fluorescence emission peak at 700–850 nm, that is attributed to the plasmonic resonance effect of Ag, instead rises as the loadings of Ag increases (Fig. 4(b)). This can be an indicator for the accumulation of more hot electrons generated by the plasmonic Ag NPs.

With the band structure established, we set to elucidate the charge dynamics on the metal/semiconductor interface by examining the photoconversions with UiO-66-$(SH)_2$ and Ag_1@UiOS under illumination of λ < 400 nm and λ > 490 nm, which correspond to the absorption ranges of plasmonic Ag NPs and UiO-66-$(SH)_2$, respectively. As shown in Fig. 4(c), the introduction of Ag brought subtle impact to the production rate of CO without C_xH_y being found at λ < 400 nm. The results exclude the interfacial electron transfer pathway from the MOFs semiconductor to Ag in the CO_2 reduction catalysis, where Ag act as the cocatalyst. At λ > 490 nm, UiO-66-$(SH)_2$ was found to be nearly inactive as anticipated, whereas Ag_1@UiOS achieved 50.0-folds increase of CO yield along with the generation of C_xH_y (1.38 μmol·g^{-1}·h^{-1}), implying that the enhancement of photocatalytic efficiency and the multiple-electron reductions predominantly stemmed from the LSPR effects of Ag NPs. The plasmonic NPs can inject hot electrons to the conduction band of semiconductor across the Schottky barrier. To confirm this pathway, we conducted the transient photocurrent response analysis of all the photocatalysts. As depicted in Fig. 4(d), the introduction of plasmonic Ag NPs results in the increase of photocurrent compared with bare UiO-66-$(SH)_2$. The positive dependence of the photocurrent on the loading amounts of Ag NPs confirms it as the light-harvesting antenna that boost the CO_2 reductions over anatase UiO-66. It is important to note that Ag_1@UiOS exhibits higher photocurrent than Ag_2@UiOS, which agrees with the photocatalytic results (Fig. 3(a)). The transient absorption (TA) spectroscopy found the induction of hot electrons with a lifetime of only 20 ps (Fig. S21 in the ESM). We therefore confirm the hot-electron injection to the MOF semiconductor as the main mechanism for the plasmon-induced deep reductions of CO_2. A photocatalytic reaction pathway is herein proposed (Fig. S22 in the ESM). The photo irradiation of plasmonic Ag NPs induces the hot electron injection to the CO_2 absorbed on

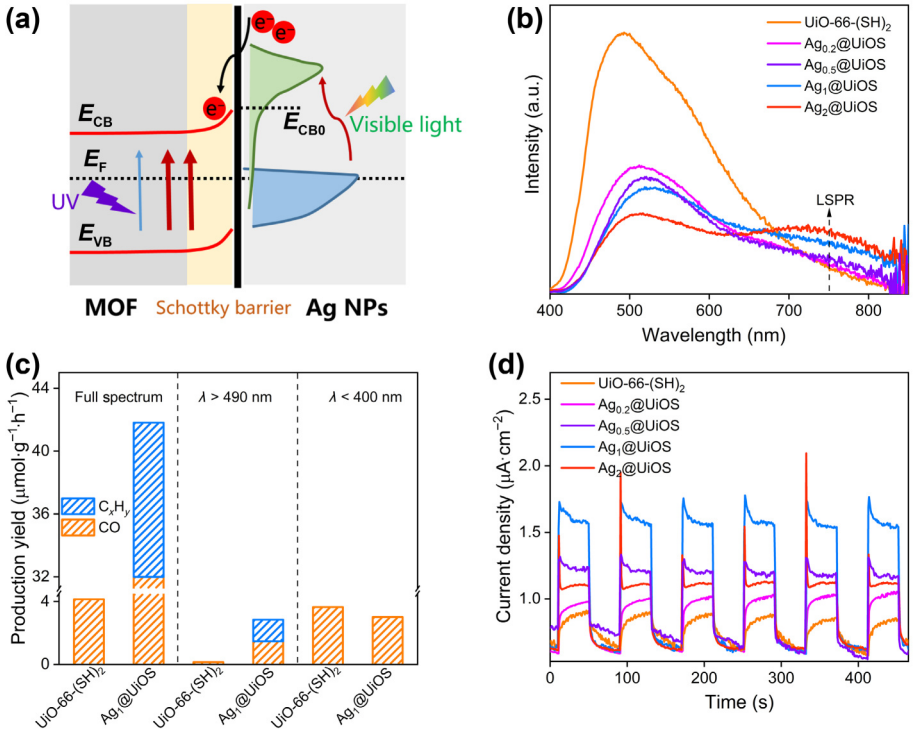

Figure 4 Mechanistic study of the enhanced CO_2 reduction performance of Ag@UiOS. (a) Diagram of Schottky barrier formation. (b) Steady-state PL spectra for UiO-66-$(SH)_2$, $Ag_{0.2}$@UiOS, $Ag_{0.5}$@UiOS, Ag_1@UiOS, and Ag_2@UiOS. (c) Comparison of the photocatalytic CO_2 reduction performance of UiO-66-$(SH)_2$ and Ag_1@UiOS under different spectrum conditions. (d) Transient photocurrent responses (TPR) in 0.2 M Na_2SO_4 electrolyte.

UiO-66-SH_2, leading to the formation of *COOH intermediate upon the synchronous transfer of a proton. A further proton-coupled hot electron injection converts *COOH to *CO. The final desorption produces CO and regenerates Ag@UiOS catalyst.

3 Conclusions

In summary, we have developed a strategy for fabricating confined Ag plasmon-MOFs composites with ultrahigh loadings up to 51.2% based on the metal-sulfur chemical interactions. The resulting Ag@UiOS photocatalyst exhibited significantly enhanced charge transfer kinetics, leading to the outstanding reaction rates for CO_2 reductions and the partial production of hydrocarbons. We also highlight that the balance between the plasmon loadings and the mass transfer of CO_2 within the pore channels is crucial to attain the optimal catalytic kinetics. The new plasmon configurations developed here may find broad applications in photocatalysis.

Electronic Supplementary Material: Supplementary material (synthetic procedure descriptions, characterization data and catalytic test methodology) is available in the online version of this article at https://doi.org/10.26599/NR.2025.94907181.

Data availability

All data needed to support the conclusions in the paper are presented in the manuscript and the Electronic Supplementary Material. Additional data related to this paper may be requested from the corresponding author upon request.

Acknowledgements

This work was financially supported by the National Natural Science Foundation of China (Nos. 22075193 and 22072101), Natural Science Foundation of Jiangsu Province (Nos. BK20221239 and BK20211306), Six Talent Peaks Project in Jiangsu Province (No. TD-XCL-006), Priority Academic Program Development (PAPD) of Jiangsu Higher Education Institutions, China Postdoctoral Science Foundation (No. 2023M742537), Postdoctoral Fellowship Program of CPSF (No. GZC20231887), and Outstanding Engineer and Training Program for Student in Soochow University.

Declaration of competing interest

All the contributing authors report no conflict of interests in this work.

Author contribution statement

J. Z. C.: Data curation, project administration, validation, writing manuscript, experimental design. Y. H. S.: Data curation, project administration, validation, experimental design. Y. H. W.: Project administration. Z. H. W.: Project administration. Z. Y. Z.: Project administration. H. H. Y.: Project administration. Z. Y. J.: Project administration. Z. D.: Project administration. W. J. Y.: Project administration, writing manuscript. Y. P.: Project administration, funding acquisition, writing manuscript. All the authors have approved the final manuscript.

Use of AI statement

None.

References

[1] Fang, S. Y.; Rahaman, M.; Bharti, J.; Reisner, E.; Robert, M.; Ozin, G. A.; Hu, Y. H. Photocatalytic CO_2 reduction. *Nat. Rev. Methods Primers* **2023**, *3*, 61.

[2] Gong, E.; Ali, S.; Hiragond, C. B.; Kim, H. S.; Powar, N. S.; Kim, D.; Kim, H.; In, S. I. Solar fuels: Research and development strategies to accelerate photocatalytic CO_2 conversion into hydrocarbon fuels. *Energy Environ. Sci.* **2022**, *15*, 880–937.

[3] Handoko, A. D.; Li, K.; Tang, J. W. Recent progress in artificial photosynthesis: CO_2 photoreduction to valuable chemicals in a heterogeneous system. *Curr. Opin. Chem. Eng.* **2013**, *2*, 200–206.

[4] Lewis, N. S. Research opportunities to advance solar energy utilization. *Science* **2016**, *351*, eaad1920.

[5] Chen, X.; Guo, R. T.; Hong, L. F.; Yuan, Y.; Pan, W. G. Research progress on CO_2 photocatalytic reduction with full solar spectral responses. *Energy Fuels* **2021**, *35*, 19920–19942.

[6] Li, T.; Huang, H. W.; Wang, S. B.; Mi, Y.; Zhang, Y. H. Recent advances in 2D semiconductor nanomaterials for photocatalytic CO_2 reduction. *Nano Res.* **2023**, *16*, 8542–8569.

[7] Xie, Z. H.; Hwang, S.; Chen, J. G. Reduction-induced metal/oxide interfacial sites for selective CO_2 hydrogenation. *SmartMat* **2023**, *4*, e1201.

[8] Serpone, N.; Emeline, A. V. Semiconductor photocatalysis-past, present, and future outlook. *J. Phys. Chem. Lett.* **2012**, *3*, 673–677.

[9] Lan, D. P.; Sheng, W. T.; Fu, Q. Q.; Ge, J. P. Enhancement of CO_2 photoreduction efficiency by supporting blue TiO_2 with photonic crystal substrate. *Nano Res.* **2023**, *16*, 9310–9317.

[10] Jiang, L. B.; Yuan, X. Z.; Pan, Y.; Liang, J.; Zeng, G. M.; Wu, Z. B.; Wang, H. Doping of graphitic carbon nitride for photocatalysis: A review. *Appl. Catal. B: Environ.* **2017**, *217*, 388–406.

[11] Goodarzi, N.; Ashrafi-Peyman, Z.; Khani, E.; Moshfegh, A. Z. Recent progress on semiconductor heterogeneous photocatalysts in clean energy production and environmental remediation. *Catalysts* **2023**, *13*, 1102.

[12] Jiao, X. C.; Zheng, K.; Hu, Z. X.; Sun, Y. F.; Xie, Y. Broad-spectral-response photocatalysts for CO_2 reduction. *ACS Cent. Sci.* **2020**, *6*, 653–660.

[13] Wang, S. B.; Han, X.; Zhang, Y. H.; Tian, N.; Ma, T. Y.; Huang, H. W. Inside-and-out semiconductor engineering for CO_2 photoreduction: From recent advances to new trends. *Small Struct.* **2021**, *2*, 2000061.

[14] Jiang, X. Y.; Huang, J. D.; Bi, Z. H.; Ni, W. J.; Gurzadyan, G.; Zhu, Y. A.; Zhang, Z. Y. Plasmonic active "hot spots"-confined photocatalytic CO_2 reduction with high selectivity for CH_4 production. *Adv. Mater.* **2022**, *34*, 2109330.

[15] Jang, Y. H.; Jang, Y. J.; Kim, S.; Quan, L. N.; Chung, K.; Kim, D. H. Plasmonic solar cells: From rational design to mechanism overview. *Chem. Rev.* **2016**, *116*, 14982–15034.

[16] Zhang, Y. C.; He, S.; Guo, W. X.; Hu, Y.; Huang, J. W.; Mulcahy, J. R.; Wei, W. D. Surface-plasmon-driven hot electron photochemistry. *Chem. Rev.* **2018**, *118*, 2927–2954.

[17] Kim, S. M.; Lee, S. W.; Moon, S. Y.; Park, J. Y. The effect of hot electrons and surface plasmons on heterogeneous catalysis. *J. Phys.: Condens. Matter* **2016**, *28*, 254002.

[18] Tahir, M.; Tahir, B.; Amin, N. A. S. Synergistic effect in plasmonic Au/Ag alloy NPs co-coated TiO_2 NWs toward visible-light enhanced CO_2 photoreduction to fuels. *Appl. Catal. B: Environ.* **2017**, *204*, 548–560.

[19] Wang, M. Y.; Ye, M. D.; Iocozzia, J.; Lin, C. J.; Lin, Z. Q. Plasmon-mediated solar energy conversion via photocatalysis in noble metal/semiconductor composites. *Adv. Sci.* **2016**, *3*, 1600024.

[20] Wu, N. Q. Plasmonic metal-semiconductor photocatalysts and photoelectrochemical cells: A review. *Nanoscale* **2018**, *10*, 2679–2696.

[21] Gao, Z. Q.; Gong, Y.; Zhu, Y. T.; Li, J. J.; Li, L.; Shi, Y. X.; Hou, M.;

Gao, X. J.; Zhang, Z. C.; Hu, W. P. Large π-conjugated indium-based metal-organic frameworks for high-performance electrochemical conversion of CO_2. *Nano Res.* **2023**, *16*, 8743–8750.

[22] Kollmannsberger, K. L.; Kronthaler, L.; Jinschek, J. R.; Fischer, R. A. Defined metal atom aggregates precisely incorporated into metal-organic frameworks. *Chem. Soc. Rev.* **2022**, *51*, 9933–9959.

[23] Yee, K. K.; Reimer, N.; Liu, J.; Cheng, S. Y.; Yiu, S. M.; Weber, J.; Stock, N.; Xu, Z. T. Effective mercury sorption by thiol-laced metal-organic frameworks: In strong acid and the vapor phase. *J. Am. Chem. Soc.* **2013**, *135*, 7795–7798.

[24] Chowdhury, S.; Sharma, P.; Kundu, K.; Das, P. P.; Rathi, P.; Siril, P. F. Systematic thiol decoration in a redox-active UiO-66-$(SH)_2$ metal-organic framework: A case study under oxidative and reductive conditions. *Inorg. Chem.* **2023**, *62*, 3875–3885.

[25] Wu, M. C.; Ouyang, C.; Ye, Z. R.; Li, S. B.; Hong, Z. L.; Zhi, M. J. Ag-CeO_2 composite aerogels as photocatalysts for CO_2 reduction. *ACS Appl. Energy Mater.* **2022**, *5*, 7335–7345.

[26] Moon, H. R.; Kim, J. H.; Suh, M. P. Redox-active porous metal-organic framework producing silver nanoparticles from Ag^I ions at room temperature. *Angew. Chem., Int. Ed.* **2005**, *44*, 1261–1265.

[27] Jiang, W. B.; Low, B. Q. L.; Long, R.; Low, J.; Loh, H.; Tang, K. Y.; Chai, C. H. T.; Zhu, H. J.; Zhu, H.; Li, Z. B. et al. Active site engineering on plasmonic nanostructures for efficient photocatalysis. *ACS Nano* **2023**, *17*, 4193–4229.

[28] Chen, L.; Li, H. Y.; Li, H. M.; Li, H. M.; Qi, W. S.; Zhang, Q.; Zhu, J.; Zhao, P.; Yang, S. D. Accelerating photogenerated charge kinetics via the g-C_3N_4 Schottky junction for enhanced visible-light-driven CO_2 reduction. *Appl. Catal. B: Environ.* **2022**, *318*, 121863.